DOI: 10.1002/ ((please add manuscript number))
Article type: Full Paper

A Targeted Functional Design for Highly Efficient and Stable Cathodes for Rechargeable Li-Ion Batteries

Guanjie He[a,c], Xiaoyu Han[a], Rujia Zou[b,], Tingting Zhao[a], Zhe Weng[c], SocMan Ho-Kimura[a], Yao Lu[a], Hailiang Wang[c], Zheng Xiao Guo[a] and Ivan P. Parkin[a,]**

Guanjie He, Dr. Xiaoyu Han, Tingting Zhao, Dr. SocMan Ho-Kimura, Yao Lu, Prof. Zheng Xiao Guo, Prof. Ivan P. Parkin

[a]Christopher Ingold Laboratory, Department of Chemistry, University College London, 20 Gordon Street, London WC1H 0AJ, U.K.,

E-mail:i.p.parkin@ucl.ac.uk

Prof. Rujia Zou

[b]State Key Laboratory for Modification of Chemical Fibers and Polymer Materials, College of Materials Science and Engineering, Donghua University, Shanghai 201620, China, E-mail:rjzou@dhu.edu.cn

Guanjie He, Dr. Zhe Weng, Prof. Hailiang Wang

[c]Department of Chemistry and Energy Sciences Institute, Yale University, 810 West Campus Drive, West Haven, Connecticut 06516, U.S.A.

Rechargeable lithium ion batteries (LIBs) are widely used for energy storage in portable devices, due to their low cost, light weight, high energy density, no memory effect, long life span and low-toxicity to the environment.[1, 2] Despite the current success, the increasing demand for better performance stimulates further improvements in LIBs, especially energy density, cycling stability and rate capability with the emergency of a new generation of electronic devices and electric vehicles. However, the energy density of LIBs is restricted by the low capacity of cathode materials.[3, 4] Most of the commercial cathode materials, such as $LiCoO_2$, $LiMn_2O_4$ and $LiFePO_4$,[5] can only allow a theoretical maximum of one Li^+ ion insertion/extraction per formula unit due to their inherent crystal structure and redox chemistry. Hence, multi-Li ion insertion/extraction cathode materials are highly desirable in order to realize the high capacity and fast charge capability of LIBs.

Vanadium pentoxide (V_2O_5) is one of the promising candidates for such requirements, due to its high theoretical capacity, low cost and ease of synthesis. Its layered structure can readily undergo insertion/extraction of multiple Li ions *via* reversible phase transformations, *i.e.* structural formula of $Li_xV_2O_5$, α phase: $x < 0.1$; ϵ phase: $0.35 < x < 0.7$; δ phase: $x = 1$; γ phase: $1 < x < 3$ and ω phase: $x = 3$.[6] When two Li ions per formula unit take part in the intercalation process, the theoretical capacity can reach 294.0 mA h g^{-1} within the voltage range of 2.0-4.0 V. However, low Li diffusion efficiency, poor electronic conductivity and poor structural stability drag down the electrochemical performance of V_2O_5.[4, 6-8] Two proposed solutions have been made. One is the design of novel V_2O_5 structures, such as nanosheets[5, 9], microspheres[10] and nanobelts[7]. Those structures can enlarge the specific surface area and improve the diffusion efficiency of Li. Recently, ultra-large V_2O_5 nanosheets that are exceptionally thin were fabricated by Liang *et al.* These nanosheets possess a high specific discharge capacity of 141 mA h g^{-1} at a current density of 0.1 A g^{-1} with 92.6 % retention after 500 cycles.[11] Another focus is to fabricate V_2O_5 based composite materials to improve the electrochemical performance. For example, V_2O_5-graphene xerogel[6], SnO_2/V_2O_5 composites[12] and V_2O_5/mesoporous carbon composites[13].

Compared with the slurry making process required above,[6-13] direct growth of nanostructures on a current collecting substrate has been shown to avoid complex processing procedures. Previous reports have shown the avoidance of the drawbacks and complicated procedures of mixing active electrode materials with binders and conductive agents to increase the endurance of the fast charge and discharge operations.[14, 15] However, there are still some common issues for the reported core-shell composite structures[4, 16-19]: 1) both the core and the shell structures take part in the electrochemical reactions for energy storage simultaneously, which will still introduce instability and unsatisfactory cycling performance of the electrodes due to relatively large volumetric changes or even dissolution of the core structures; and 2) active materials are partially wrapped by inert protective materials, reducing their effectiveness.

With consideration of the above and further guidance from our computational simulations, we developed an integrated approach to design and synthesize a V_2O_5 coated $NiCo_2O_4$ nano-network structure supported by carbon cloth, 3D $NiCo_2O_4$@V_2O_5 core-shell arrays (CSAs). ~~The $NiCo_2O_4$ nanosheet network is first grown onto the carbon cloth support structure and then the optimised thickness of layered V_2O_5 is coated onto the $NiCo_2O_4$ network. This approach effectively separates the characteristic roles of high Li incorporation in V_2O_5 and electronic conduction *via*. $NiCo_2O_4$ and carbon cloth. Meanwhile, the volume change of V_2O_5 during lithiation/delithiation is fully accommodated by the robust $NiCo_2O_4$ nanosheet network, without exerting undue stress on the carbon cloth.~~ The carbon cloth strongly supporting the $NiCo_2O_4$ nanosheet network that acts as a robust framework and provides electron conductive channels for the whole structure, and it remains mechanically and chemically stable over the high voltage range, 2.0 - 4.0 V *vs.* Li^+/Li, even after long-term cycles. The V_2O_5 coating solely participated in lithiation/delithiation. Such structural design ensures concerted optimization of capacity, conductivity and structural stability, which are the major issues of the cathode of Li ion batteries. The whole structure reached the theoretical predicted capacity and has among the best reported cycling stability of electrodes for LIBs. Furthermore *in-situ* TEM study and theoretical simulations also provide insights into the robustness of the nanomaterials and the mechanism of the layer effects in these rational structures, which will guide V_2O_5 based LIBs studies in the future. This free-standing electrode provides a series of advantages: flexibility; large surface area; easy access of electrolyte; and efficient electron/ion transport capability. Those also show potential applications as cathodes for foldable/flexible Li-battery devices.

The schematic procedure of generating the $NiCo_2O_4@V_2O_5$ CSAs/carbon cloth was illustrated in **Figure 1**a and elaborated in details in the Experimental section in the supporting information. The flexible conductive carbon cloth, with potential applications for wearable LIB devices, were chosen as the current collector to support the whole electrodes. Firstly, $NiCo_2O_4$ nano-network was synthesized on the chosen substrate by a simple hydrothermal method followed by annealing to enhance the crystallinity, bonding and hence electron conductivity. Those porous network structure provides strong support and binding with the V_2O_5 shell. More importantly, $NiCo_2O_4$ nanostructure possesses much better electron conductivity, 5~6 orders of magnitudes higher than that of V_2O_5[20-23]. The nano-architectured design also benefits from the open channels of 3D $NiCo_2O_4$ nanostructure which are easy to access by the electrolyte and hence enable efficient ion transfer. Secondly, V_2O_5 nanosheets were coated on both sides of the $NiCo_2O_4$ nanosheets arrays by the hydrothermal method and formed a well-connected core-shell network structure. The strong structure and the binding between the structure and the carbon-support partially alleviates the possible stress of volume expansion from the lithiation process. In order to obtain the best electrochemical performances, different concentrations of reaction solution (0.1~0.4 mL) were adjusted to identify the appropriate thickness ratio of the core-shell network.

The morphologies of the pure carbon cloth, $NiCo_2O_4$/carbon cloth and those of $NiCo_2O_4$@V_2O_5 CSAs/carbon cloth were determined by SEM. The pure carbon fibers are interweaved and formed cloth with a surface structure facilitating heterogeneous nucleation of the $NiCo_2O_4$ (Figure S1). After the initial reaction, $NiCo_2O_4$ nanosheets were grown over the individual carbon fibers to form a nano-network with a mesoporous structure (Figure S2). For the growth of V_2O_5 shell on the $NiCo_2O_4$ core, when the pre-reaction solution was at 0.1 mL, the morphologies of the nanosheets become rough with small nanoparticles adhered on the surfaces (Figures S3a, 1b). When the concentration of the precursor solution was increased to 0.2 mL, V_2O_5 nanosheets were observed that were capped on both sides of the $NiCo_2O_4$ sheets forming sandwich structures (Figures S3b, 1c). Further increases of the vanadium oxytriisopropoxide solution to 0.3 and 0.4 mL, the thickness of the V_2O_5 nanosheets increased dramatically (Figures S3c, 3d and Figures 1d, 1e). A mass of the nanosheets stack together and even block the porous structures, thus retarding the Li^+ ion diffusion and electron transfer during electrochemical reactions.

The detailed topography and microstructure of the sandwich-like structures were further analyzed by transmission electron microscopy (TEM). From the low magnification TEM image (**Figure 2**a), the nanosheets show clearly the mesoporous structure with pore sizes of several hundred nanometers to micrometers. A high magnification TEM image in Figure 2b shows more clearly the nanosheet morphology of the structure. Such structures provide high specific open surface areas for easy soaking of the electrolyte, and fast transfer of ions and electrons. The mesoporous structures can be detected on the individual nanosheet. High resolution TEM (HRTEM) image of the interface between $NiCo_2O_4$ and V_2O_5 is shown in Figure 2c, where the lattice space of ~0.234 nm corresponds to the (222) plane of the $NiCo_2O_4$ spinel structure, and the lattice spacing of ~0.265 and ~0.438 nm can be indexed to the (310) and (001) planes of the V_2O_5 orthorhombic structure, respectively. The heterostructures formed strong coherency across the interface, due to the relatively small lattice mismatch, which ensures the sandwich structure integrity to facilitate large levels of Li^+ insertion/extraction. The crystallographic phases of the $NiCo_2O_4$@V_2O_5 CSAs/carbon cloth were further characterized by X-ray diffraction (XRD), Figure 2d, where the two main diffraction peaks at 14.1° and 20.2° are indexed to the (110) crystal planes of the orthorhombic phase of V_2O_5 and (400) crystal plane of the spinal phase $NiCo_2O_4$, respectively. A series of relatively weak and somewhat broad peaks can be indexed to V_2O_5 (JCPDS no. 41-1426) and $NiCo_2O_4$ (JCPDS no. 20-0781), respectively. Furthermore, the phase of V_2O_5 powder samples was recorded by XRD in Figure S4b, which showed more evident diffraction peaks with smaller width at half maxima intensity that corresponded to the orthorhombic phase of V_2O_5. The elemental distribution of the $NiCo_2O_4$@V_2O_5 CSAs was detected by X-ray mapping with a matching TEM image, this revealed that Ni, Co, V and O are uniformly distributed in the core (Ni, Co, O) and the shell (V, O) regions, which is in accordance with the X-ray photoelectron spectroscopy (XPS) spectra (Figure S5).

The electrochemical properties of the four $NiCo_2O_4$@V_2O_5 CSAs as the cathodes for LIBs were evaluated, **Figure 3**. The cycling performance was investigated under a current density of 0.5 C for 100 cycles as shown in Figure 3a. As expected, sandwich-structural $NiCo_2O_4$@V_2O_5 CSAs, sample 1c, shows the best performance with the highest discharge capacity of ~276.4 mA h g^{-1}, calculated by the total mass of $NiCo_2O_4$ framework and V_2O_5 active material, compared with other samples (discharge capacity of ~238.9 mA h g^{-1}, ~197.3 mA h $g^{-1}$and ~166.8 mA h g^{-1} for sample 1b, 1d and 1e, respectively). The results indicate that the thickness of the V_2O_5 nanosheet out-layers affects the specific capacity. The following electrochemical performance was carried out using the sandwich-structural $NiCo_2O_4@V_2O_5$ CSAs unless stated otherwise.

The CV curves of the first and second cycles at a scan rate of 0.1 mV s^{-1} in the voltage window of 2.0 - 4.0 V *vs.* Li/Li^+ are shown in Figure 3b. In the second stable cycle, the first cathodic peak at 3.34 V can be indexed to phase changes from α-$Li_xV_2O_5$ ($x<0.1$) to ε-$Li_{0.5}V_2O_5$. Other two reduction peaks at 3.13 and 2.23 V can be attributed to the formation of δ-LiV_2O_5 and ɤ-$Li_2V_2O_5$, respectively. In the Li de-intercalation process, three anodic peaks observed at 2.52, 3.28 and 3.48 V correspond to the reverse phase transformations, i.e. from ɤ-$Li_2V_2O_5$, δ-LiV_2O_5, ε-$Li_{0.5}V_2O_5$ to α-$Li_xV_2O_5$ ($x<0.1$), respectively. There are no other peaks from the CV curves, suggesting only the V_2O_5 phase transformations take place in the electrochemical reactions. This also indicates the stability of the network structure during the whole electrochemical process. The reaction steps can be expressed in the following[3]:

$V_2O_5 + 0.5\ Li^+ + 0.5e^- \leftrightarrow \varepsilon\text{-}Li_{0.5}V_2O_5$ Equation (1)

$\varepsilon\text{-}Li_{0.5}V_2O_5 + 0.5\ Li^+ + 0.5\ e^- \leftrightarrow \delta\text{-}LiV_2O_5$ Equation (2)

$\delta\text{-}LiV_2O_5 + Li^+ + e^- \leftrightarrow \gamma\text{-}Li_2V_2O_5$ Equation (3)

Figure 3c shows the first, second and fifth cycles of the CD profiles for the $NiCo_2O_4@V_2O_5$ CSAs at a current density of 0.1 C. After the first cycle to form the solid state electrolyte interface layer, the capacity remains stable and then slowly decreases. As shown in the figure, there is no evident flat voltage plateaus in the charge and discharge curves, which corresponds with a relatively low crystallinity of the V_2O_5 structure. It is demonstrated that lower crystallinity can lead to less stress on the electrodes during the Li ion insertion/extraction and better cyclic performance. In line with the above CV results, three distinct voltage stages could be observed at 3.40-3.32, 3.15-3.10 and 2.35-2.23 V on the discharge curves. Those stages represent the Li ion intercalation processes. Likewise, three corresponding voltage stages at 2.42-2.55, 3.20-3.35 and 3.42-3.53 V are related to the Li ion de-intercalation processes. Both CV and CD results confirm the multi-step Li intercalation process.

Rate capabilities of the $NiCo_2O_4@V_2O_5$ CSAs are shown in Figure 3d. A stable discharge capacity of 292.0 mA h g^{-1} was delivered at a current density of 0.1 C, with increasing current density, the discharge capacity decreases to 256.8, 198.4, 151.9 and 128.7 mA h g^{-1}, respectively at 1.0 C, 5.0 C, 10 C and 20 C. It is noted that the electrodes show good rate performance with ~ 45% retention when the current density is increased by 200 times. This is higher than a large series of reported cathode nanostructures for LIBs (Table S1). The specific discharge capacity of 271.6 mAh g^{-1} can be maintained when the current density was recovered to 0.1C after 60 cycles of stepwise current density changes, corresponding to a capacity retention of ~ 93.0 % of its initial value. These improvements can be attributed to the complete Li intercalation/de-intercalation reaction of the V_2O_5 coating and rapid charge and Li^+ transfer within the whole heterostructure. The specific discharge capabilities of the $NiCo_2O_4$ nanosheet are shown in Figure S6. These contribute negligible capabilities of 14.6 and 6.9 mAh g^{-1} at current densities of 0.1 C and 1 C, respectively. It can be concluded that the "core" $NiCo_2O_4$ shows no electrochemical reactions with Li^+ within the voltage range of 2.0-4.0 V *vs*. Li^+/Li and this largely insignificant capacity is from the limited ion absorption on the surface of the nanosheets.

To tackle the persistent challenge of unsatisfied cyclic stability, the $NiCo_2O_4@V_2O_5$ CSAs electrode was evaluated under 500 cycles of a cyclic CD test at a high current density of 10 C, Figure 3e. Impressively, except for the first few cycles, the cycling stability was largely maintained with only 0.0126 % capacity loss per cycle within 500 cycles and with a Coulombic efficiency > 99.5 %. For comparison, flower-like V_2O_5 nanoparticles (SEM in

Figure S4a) and V_2O_5/carbon clothes were fabricated into coin cells as cathodes for LIBs. After 500 cycles under the same conditions, the capacities retained are 40.7% and 33.5% of their initial value, respectively, equivalent to 0.12% and 0.13% capacity decay per cycle. Hence, $NiCo_2O_4$@V_2O_5 CSAs/carbon cloth improved the cycling stability by 10 times, compared with the V_2O_5 nanoparticles and V_2O_5/carbon cloth synthesized by the same procedure. All these results demonstrate the excellent cyclic stability and reversibility with no side reactions in the $NiCo_2O_4$@V_2O_5 SAs/carbon cloth electrodes. Compared with the literatures, the exceptional cycling performance of the $NiCo_2O_4$@V_2O_5 CSAs/carbon cloth electrodes is among the best reported nanostructures for cathodes of LIBs (Table S1). This long lifetime was consistent with the almost unchanging morphology of the morphology after 500 cycles: though the sandwich network became relatively thick, Figure S8a, the porous structures of $NiCo_2O_4$@V_2O_5 CSAs structure remains intact. As for powdery V_2O_5 samples, the surface appeared to be rough with the nanoparticles further stacking together, Figure S8b, which reduces the electrolyte accessibility and the electrochemical intercalation processes. The extraordinary performance stability and the morphologies further verify the successful benefit from the rational design and the robustness of the open network structure.

As mentioned before, poor structural stability, inferior electron conductivity and sluggish Li diffusivity are the main issues of the V_2O_5 nanosheet cathodes for LIBs. The first issue, *i.e.* structural instability, mainly originated from the strains induced by the volumetric expansion of the electrochemical active material during the lithiation process. It can lead to fracture, falling off and electrical disconnection with the framework or the current collector, which will shorten the service life of LIBs. *In-situ* TEM observation was carried out to detect the mechanical properties and morphology evolution of $NiCo_2O_4$@V_2O_5 CSAs during Li intercalation and de-intercalation from the V_2O_5 layers, using a dual-probe biasing TEM holder, as shown in **Figure 4**a. $NiCo_2O_4$@V_2O_5 CSAs were assembled on a Pt wire probe, the opposite was an Au wire probe decorated with a small piece of Li/Li_2O. By controlling a piezoelectric motor on the TEM holder, the $NiCo_2O_4$@V_2O_5 CSAs contacted with Li/Li_2O, and a bias voltage of -4.0 V was applied to drive Li ion to go through the solid-state electrolyte towards $NiCo_2O_4$@V_2O_5 CSAs. Figure 4b shows the pristine $NiCo_2O_4$@V_2O_5 CSAs before the lithiation. Figure 4c shows that $NiCo_2O_4$@V_2O_5 CSAs went through lithiation process for 15 min, where the coated structure continues to expand. After 30 min (Figure. 4d), there's negligible further expansion and this verifies that the reaction is complete. The major volumetric expansion period is in the initial 15 min. The *ca.* 1.22 times of volume change can be detected, compared with its initial state. The delithiation process was also recorded (Figure S9) after 30 min. Compared with its initial state, an increase thickness of the coating is due to the distortion of V_2O_5 during lithiation/delithiation. It is noted that there is no cracking or fracture in the $NiCo_2O_4$@V_2O_5 CSAs during the whole process of lithiation. As expected, the $NiCo_2O_4$@V_2O_5 CSAs showed slight volumetric expansion and the $NiCo_2O_4$ core structure possesses sufficient ductility to accommodate the volumetric expansion, which protects the whole structure during lithiation process. The whole electrochemical process demonstrates clearly the structural stability and the excellent cycling performance of these sandwich structures. These results were in line with the SEM images before and after long term cycling.

To further understand and tackle the issue of sluggish Li diffusivity within the layered V_2O_5, we carried out theoretical calculations to study the Li intercalation in layered α-V_2O_5 using Density Functional Theory (DFT) approaches, details of which is given in the experimental section in the supporting information. First, the simulated lattice parameters and the V-O bond distances of the α-V_2O_5 structure (**Figures 5**a, 5b and S10) as a result of different functionals were compared with the experimental and other theoretical data and shown in Table S2. In previous calculations, the *c* vector, the stacking direction, is heavily overestimated, even by

9.98 %,[24, 25] because the van der Waals contributions are not adequately considered in the standard DFT calculations. This is in fact very important for layered structures.[26] The discrepancy of such predictions with experimental values are indeed rather large, as shown in Table S2. Moreover, the PBEsol functional has proven to yield property predictions of densely packed materials and their surfaces.[27] The results indeed compare favourably with experiment that the error of the lattice parameters was under 0.55%. Hence, the PBEsol-vdW-DF functional should be highly appropriate to predict the geometries of α-V_2O_5, which is critical for further calculation as its high thermal expansion coefficients.[28] This functional was hence selected in subsequent calculations.

The calculated electronic density of states (DOS) of α-V_2O_5 are shown in Figure S10. The calculated direct band gap at Gamma point is 2.55 eV, whereas the indirect band gap is 1.98 eV, which is consistent with previous calculations[24] and experimental results.[29-31] The partial charge density of the valence band maximum (VBM) and the conduction band minimum (CBM) are shown in Figures 5a and 5b, where the VBM is mainly centred on vanadium, consisting of $3d_{xy}$ orbitals and the CBM is concentrated on the oxygen atoms.

Before discussion of the Li diffusion through the α-V_2O_5, the stable insertion sites of Li in α-V_2O_5 were studied, which are denoted as the upper and the lower hollow sites H_a and H_b and the top site T. The binding energy is calculated according to the following equation:

$$E_b = E_{total} - (E_{V_2O_5} + E_{Li}) \qquad \text{Equation (4)}$$

where E_{total} is the energy of the whole system, $E_{V_2O_5}$ and E_{Li} are the energies of the pristine layered V_2O_5 and the chemical energy of a single Li, respectively. Our results (Table S3) suggest that the upper hollow site H_a is all over the most stable site, followed by the top site T. The lower site H_b is the least favourable site to be inserted. This conclusion is in accordance with previous work.[24, 32] Meanwhile, the layer effect also plays a role in the binding energy.

The deeper the Li is inserted, the higher the binding energy E_b. This suggests that the Li atom is keen to bind with the top layers of the α-V_2O_5 slab.

As for the Li diffusion in the layered α-V_2O_5, two different pathways have been considered, as illustrated in Figures 5c and 5d. Diffusion within the layers has been intensively studied in previous theoretical reports.[24, 32,-34] However, the study on the other pathway where Li diffuse across the layered α-V_2O_5 has not been reported yet, neither has the layer effect on the Li diffusivity. For Li diffusion in the non-interaction lattice, the diffusion coefficient can be simply obtained through $\mathrm{D} = \Gamma \times d^2$, where Γ and d are the hopping frequency and hopping distance, respectively.[35] Further by adopting the Arrhenius theory and the transition state theory, the equation of diffusivity can be put together in the following equation:[36]

$$D = d^2 v^* e^{-\frac{E_{act}}{k_B T}} \qquad \text{Equation (5)}$$

where E_{act} is the activation energy, v^* is the attempt frequency, k_B and T are the Boltzmann constant and temperature respectively. As for the activation energy E_{act} of a Li atom to diffuse through the α-V_2O_5, it can be simplified as the energy barrier along the diffusion pathway. Whereas the attempt frequency v^* is generally in the range of phonon frequencies.[37] This is adopted from the experimental data of the literature[38], where $v* = 3.1 \times 10^{13}$ Hz.

The simulated Li average diffusivities along the two different pathways for few layers α-V_2O_5 are shown in Figure 5e. Overall, the in-plane diffusivity is far higher than the inter-plane intercalation by 12 orders of magnitude. The in-plane diffusivity varies exponentially with the thickness, $\sim e^{0.4835x}$, where x is the thickness of V_2O_5 layers. As for individual diffusivity in different layers, the intercalation along the top layer possesses the highest diffusivity. This is due to the lower energy penalty needed to hop from one hollow position to another within the same layer on the surface of the α-V_2O_5 slab. As the layer thickness increases, the binding energy and energy barrier of Li drops, leading to an increased diffusion rate on the surface. As for intercalation in the middle of the slides, the diffusivity drops considerably. The situation is similar to the bulk, where the Li binds to both the upper and the lower layers. Even though the over-all diffusivity is dominated by the in-plane pathway, the inter-plane diffusion plays the key role in incorporating more Li from the solution into the layered α-V_2O_5, *i.e.* contributing to capacity. Our results show that the inter-plane diffusion is declined by ~ $x^{-3.3474}$. And two formulas were fitted according to the simulated results of 5 layers of α-V_2O_5 in Table S4.

As calculated from the high magnification SEM images of $NiCo_2O_4@V_2O_5$ CSAs and 3D $NiCo_2O_4$ nanosheets arrays (Figure S12), the thickness of the outer layers of V_2O_5 from 3D sandwich structures are ~ 32.6 nm, which is equivalent to ~ 77 atomic layers of V_2O_5. The corresponding inter-plane diffusivity of Li for the innermost layer can be estimated as ~ 3.72×10^{-26} cm^2 S^{-1}. The ideal relationship between the thickness of the V_2O_5 layers and the specific capacity is shown in Figure 5f. The mass of the conductive and supporting frameworks with negligible contributions to specific capacity, *i.e.* 3D networked $NiCo_2O_4$, was summed with active materials. With the increase of thickness of the V_2O_5 active materials and keeping the mass of the frameworks constant, the mass loading would increase sharply and the sum of the specific capacity can approach the theoretical values of the V_2O_5 even without considering the Li diffusion limitations and electrical conductivity. Obviously, the rapid decline of diffusion of Li within V_2O_5 layers is the main limitation for realizing the theoretical specific capacity. In this 3D sandwich structures, the above calculated inter-plane diffusivity value together with the enhanced electrical conductivity (Figure S13, 14 and Table S5) can guarantee the realizing of theoretical specific capacity at the current density of 0.1 C.

In summary, a targeted functional design of sandwich-structural 3D $NiCo_2O_4@V_2O_5$ CSAs on carbon cloth as the cathode for LIBs have been balanced the major issues in the cathode improvements and shown excellent specific capacity of ~ 292.0 mA h g^{-1} at a current density of 0.1 C, superior rate capability of ~ 45 % retention when the current density was increased 200 times based on the total mass of active materials and frameworks and one of the best reported cycling performances of 0.0126% capacity decrease per cycle over 500 cycles. The rational structure design was proved from both *in-situ* TEM and theoretical simulation works. The DFT calculations gave the quantum level insights of the layer effect on the Li diffusion in the layered α-V_2O_5. By studying the few layer slides of both in-plane and inter-plane pathway, our results suggest that the speed of diffusivity of Li is dominated by the in-plane direction, whereas inter-plane direction diffusion affects further more Li intercalation. The balance of the Li diffusivity and the specific capacity of the electrode materials can reach to an optimized level. The impact of this work is that it can expand the scope of the design concept of nanostructures for electrodes for batteries and shows that layered V_2O_5 nanostructures have an exciting future for LIBs cathodes application.

Acknowledgements

G. He. and X. Han contributed equally to this work. University College London and China Scholarship Council are acknowledged for UCL-CSC joint Ph.D scholarship. UCL Doctoral School is acknowledged for Yale-UCL Collaborative Bursary. The authors would like to thank the financial support from Engineering and Physical Sciences Research Council (EPSRC), the ‘‘Pujiang’’ Program of Shanghai Education Commission (Grant No. 16PJ1400200), National Natural Science Foundation of China (Grant No. 51672044) and DHU Distinguished Young Professor Program to carry out the experiments and our membership of the UK’s HPC Materials Chemistry Consortium, which is funded by EPSRC (EP/L000202). The authors would also thank the use of the UCL Grace High Performance Computing Facility and associated support services, in the completion of this work.

Supporting Information

Supporting Information is available online from the Wiley Online Library or from the author.

Received: ((will be filled in by the editorial staff))
Revised: ((will be filled in by the editorial staff))
Published online: ((will be filled in by the editorial staff))

References:

[1] J. -M. Tarascon, M. Armand, *Nature* **2001**, *414*, 359.

[2] V. Etacheri, R. Marom, R. Elazari, G. Salitra, D. Aurbach, *Energy Environ. Sci.* **2011**, *4*, 3243.

[3] D. Chao, X. Xia, J. Liu, Z. Fan, C. F. Ng, J. Lin, H. Zhang, Z. X. Shen, H. J. Fan, *Adv. Mater.* **2014**, *26*, 5794.

[4] D. Kong, X. Li, Y. Zhang, X. Hai, B. Wang, X. Qiu, Q. Song, Q.-H. Yang, L. Zhi, *Energy Environ. Sci.* **2016**, *9*, 906.

[5] X. Peng, X. Zhang, L. Wang, L. Hu, S. H.-S. Cheng, C. Huang, B. Gao, F. Ma, K. Huo, P. K. Chu, *Adv. Funct. Mater.* **2016**, *26*, 784.

[6] Q. Liu, Z. F. Li, Y. Liu, H. Zhang, Y. Ren, C. J. Sun, W. Lu, Y. Zhou, L. Stanciu, E. A. Stach, J. Xie, *Nat. Commun.* **2015**, *6*, 6127.

[7] X. Rui, Y. Tang, O. I. Malyi, A. Gusak, Y. Zhang, Z. Niu, H. T. Tan, C. Persson, X. Chen, Z. Chen, Q. Yan, *Nano Energy* **2016**, *22*, 583.

[8] M. Chen, X. Xia, J. Yuan, J. Yin, Q. Chen, *J. Power Sources* **2015**, *288*, 145.

[9] X. Rui, Z. Lu, H. Yu, D. Yang, H. H. Hng, T. M. Lim, Q. Yan, *Nanoscale*, **2013**, *5*, 556.

[10] S. Wang, Z. Lu, D. Wang, C. Li, C. Chen, Y. Yin, *J. Mater. Chem.* **2011**, *21*, 6365.

[11] S. Liang, Y. Hu, Z. Nie, H. Huang, T. Chen, A. Pan, G. Cao, *Nano Energy* **2015**, *13*,

58.

[12] G. Yang, H. Song, M. Wu, C. Wang, *Electrochim. Acta* **2016**, *205*, 153.

[13] M. Ihsan, Q. Meng, L. Li, D. Li, H. Wang, K. H. Seng, Z. Chen, S. J. Kennedy, Z. Guo, H.-K. Liu, *Electrochim. Acta* **2015**, *173*, 172.

[14] R. Zou, Z. Zhang, M. F. Yuen, M. Sun, J. Hu, C.-S. Lee, W. Zhang, *NPG Asia Mater.* **2015**, *7*, e195.

[15] G. He, J. Li, W. Li, B. Li, N. Noor, K. Xu, J. Hu, I. P. Parkin, *J. Mater. Chem. A* **2015**, *3*, 14272.

[16] G. Kucinskis, G. Bajars, J. Kleperis, *J. Power Sources* **2013**, *240*, 66.

[17] L. Zhan, S. Wang, L.-X. Ding, Z. Li, H. Wang, *J. Mater. Chem. A* **2015**, *3*, 19711.

[18] B. Sun, K. Huang, X. Qi, X. Wei, J. Zhong, *Adv. Funct. Mater.* **2015**, *25*, 5633.

[19] B. Yan, X. Li, Z. Bai, Y. Zhao, L. Dong, X. Song, D. Li, C. Langford, X. Sun, *Nano Energy* **2016**, *24*, 32.

[20] H. Song, C. Zhang, Y. Liu, C. Liu, X. Nan, G. Cao, *J. Power Sources* **2015**, *294*, 1.

[21] M. Castriota, E. Cazzanelli, A. Fasanella, D. Teeters, *Thin Solid Films* **2014**, *553*, 127.

[22] H. Yu, X. Rui, H. Tan, J. Chen, X. Huang, C. Xu, W. Liu, D. Y. Yu, H. H. Hng, H. E. Hoster, Q. Yan, *Nanoscale* **2013**, *5*, 4937.

[23] G. Q. Zhang, H. B. Wu, H. E. Hoster, M. B. Chan-Park, X. W. Lou, *Energy Environ. Sci.* **2012**, *5*, 9453.

[24] J. Carrasco, *J. Phys. Chem. C* **2014**, *118*, 19599.

[25] D. O. Scanlon, A. Walsh, B. J. Morgan, G. W. Watson, *J. Phys. Chem. C* **2008**, *112*, 9903.

[26] X. Han, H. M. Stewart, S. A. Shevlin, C. R. Catlow, Z. X. Guo, *Nano Lett.* **2014**, *14*, 4607.

[27] J. P. Perdew, A. Ruzsinszky, G. I. Csonka, O. A. Vydrov, G. E. Scuseria, L. A. Constantin, X. Zhou, K. Burke, *Phys. Rev. Lett.* **2008**, *100*, 136406.

[28] J. J. Krochmal, *J. Am. Ceram. Soc.* **1965**, *48*, 328.

[29] N. V. Hieu, *J. Vac. Sci. Technol.* **1981**, *18*, 49.

[30] S. F. Cogan, N. M. Nguyen, S. J. Perrotti, R. D. Rauh, *J. Appl. Phys.* **1989**, *66*, 1333.

[31] A. Z. Moshfegh, A. Ignatiev, A. *Thin Solid Films* **1991**, *198*, 251.

[32] Z. Wang, Q. Su, H. Deng, *Phys. Chem. Chem. Phys.* **2013**, *15*, 8705.

[33] G. S. Gautam, P. Canepa, R. Malik, M. Liu, K. Persson, G. Ceder, *Chem. Commun. (Camb.)* **2015**, *51*, 13619-13622.

[34] W. Y. Ma, B. Zhou, J. F. Wang, X. D. Zhang, Z. Y. Jiang, *J. Phys. D: Appl. Phys.* **2013**, *46*, 105306.

[35] R. Kutner, *Phys. Lett. A* **1981**, *81A*, 239.

[36] K. A. Connors, *Wiley* **1990**.

[37] G. H. Vineyard, *J. Phys. Chem. Solids* **1957**, *3*, 121.

[38] P. Clauws, J. Vennik, *Phys. Stat. Sol. B* **1976**, 76, 707.

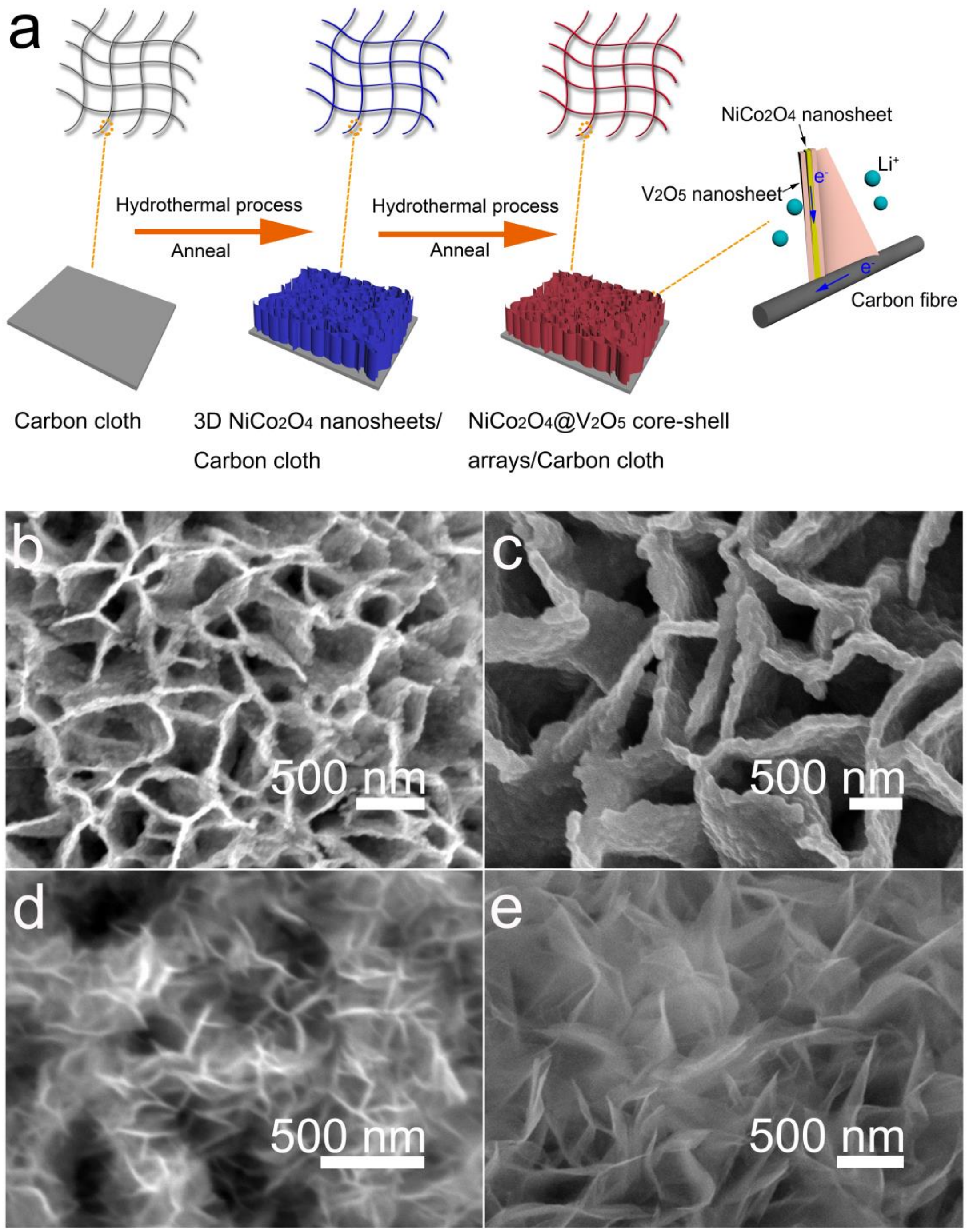

Figure 1. Synthesis procedure and the morphologies of the products. (a) Schematic illustration of the synthesis process for $NiCo_2O_4@V_2O_5$ core-shell arrays (CSAs) on carbon cloth; (b-e) SEM images of four $NiCo_2O_4@V_2O_5$ CSAs on carbon cloth with different reaction solution concentrations (b: 0.1 mL, c: 0.2 mL, d: 0.3 mL and e: 0.4 mL of vanadium oxytriisopropoxide, respectively) in the second hydrothermal process of (a).

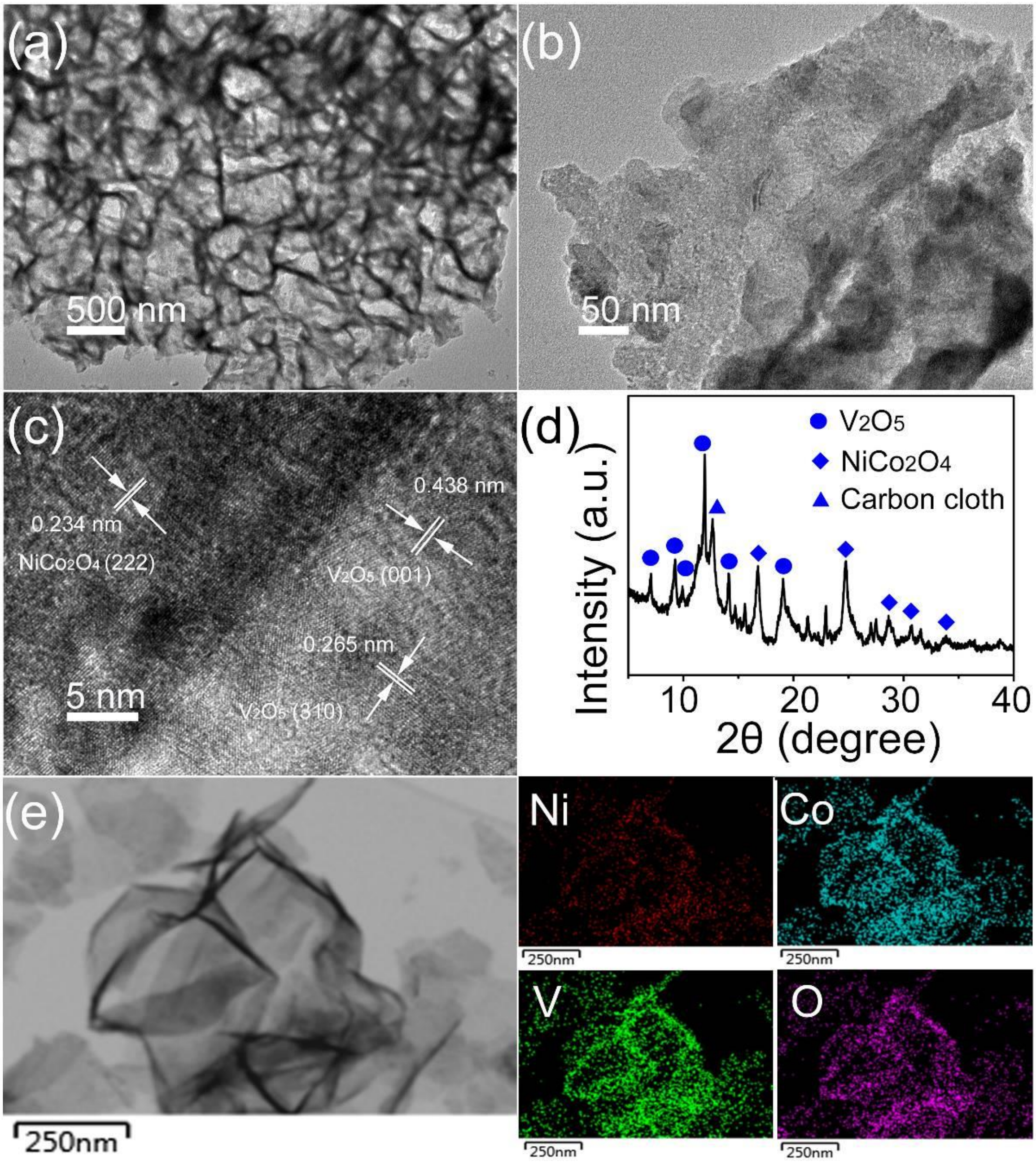

Figure 2. Structural characterization of the $NiCo_2O_4@V_2O_5$ CSAs. (a) Low and (b) high magnification TEM images of $NiCo_2O_4@V_2O_5$ CSAs; (c) High resolution TEM images of $NiCo_2O_4@V_2O_5$ CSAs; (d) XRD pattern of $NiCo_2O_4@V_2O_5$ CSAs/carbon cloth; (e) TEM images with corresponding elemental maps.

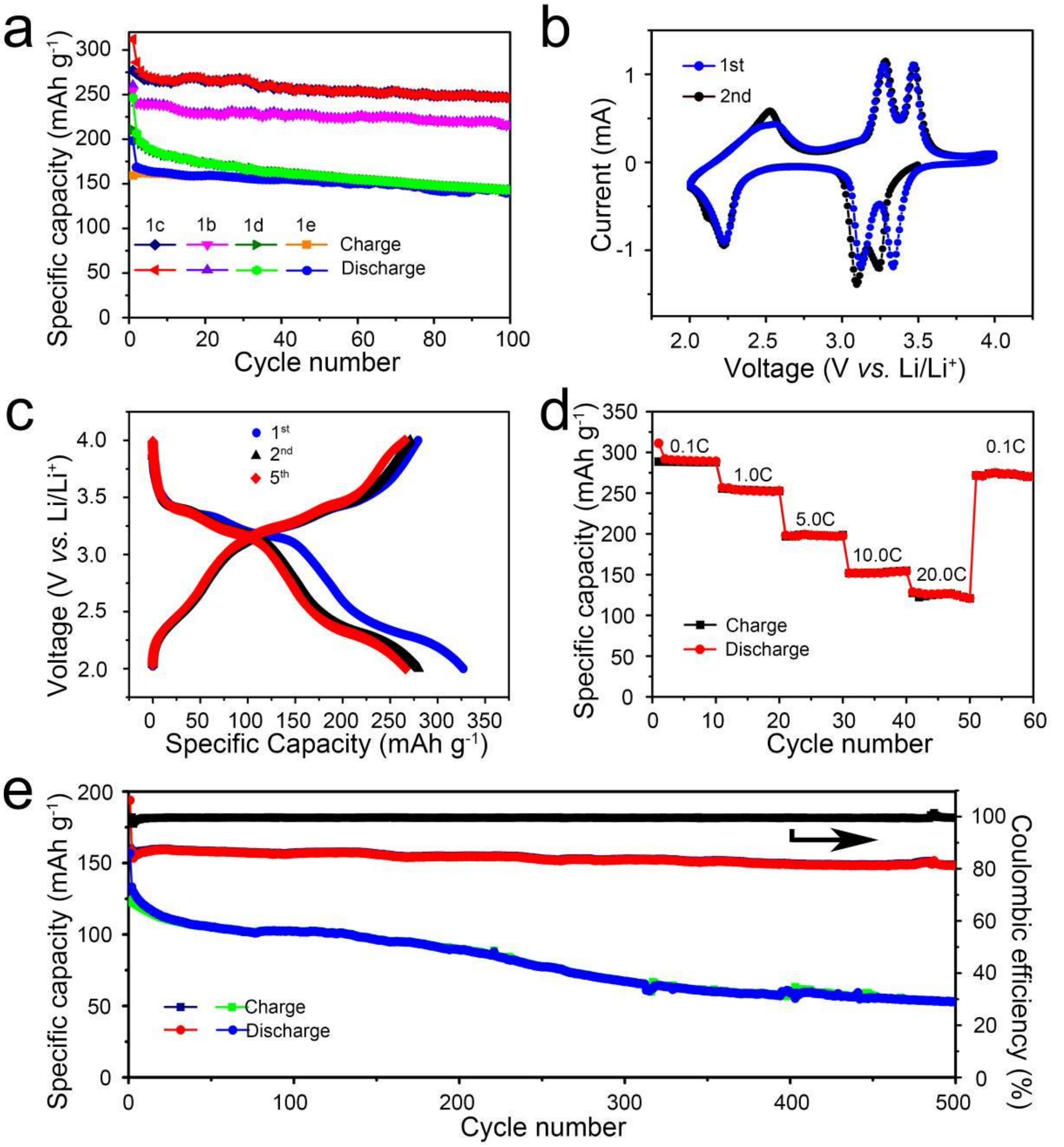

Figure 3. Electrochemical performances over the $NiCo_2O_4@V_2O_5$ CSAs as cathodes for LIBs. (a) Cycling performances of four $NiCo_2O_4@V_2O_5$ CSAs at a current density of 0.5 C (1b, 1c, 1d and 1e corresponding to different samples in Figure 1b, 1c, 1d and 1e); (b) Cyclic voltammetry (CV) test of $NiCo_2O_4@V_2O_5$ CSAs at a scan rate of 0.1 mV s^{-1}; (c) Charge-discharge curves (CD) of $NiCo_2O_4@V_2O_5$ CSAs at a current density of 0.1C. (d) Rate performances of $NiCo_2O_4@V_2O_5$ CSAs at various current densities; (e) Cycling performance and corresponding Coulombic efficiency of $NiCo_2O_4@V_2O_5$ CSAs and cycling performance of V_2O_5 nanoparticles measured at high current density of 10 C.

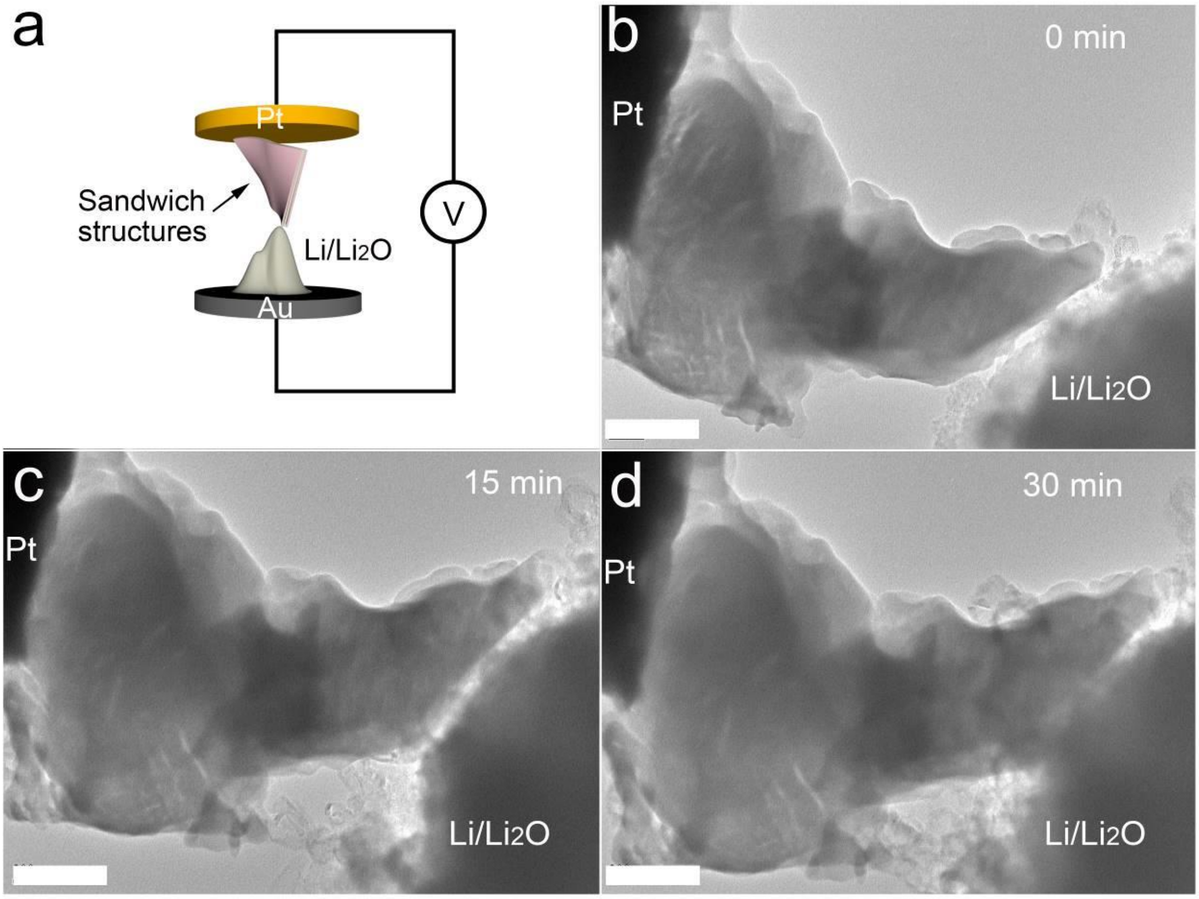

Figure 4. Structural design discussion based on *in-situ* TEM. (a) Schematic diagram showing the configuration of *in-situ* TEM observations of the lithiation process; (b-d) TEM images monitoring the lithiation process of the $NiCo_2O_4@V_2O_5$ CSAs at 0, 15 and 30 min, respectively (Scale bar: 500 nm).

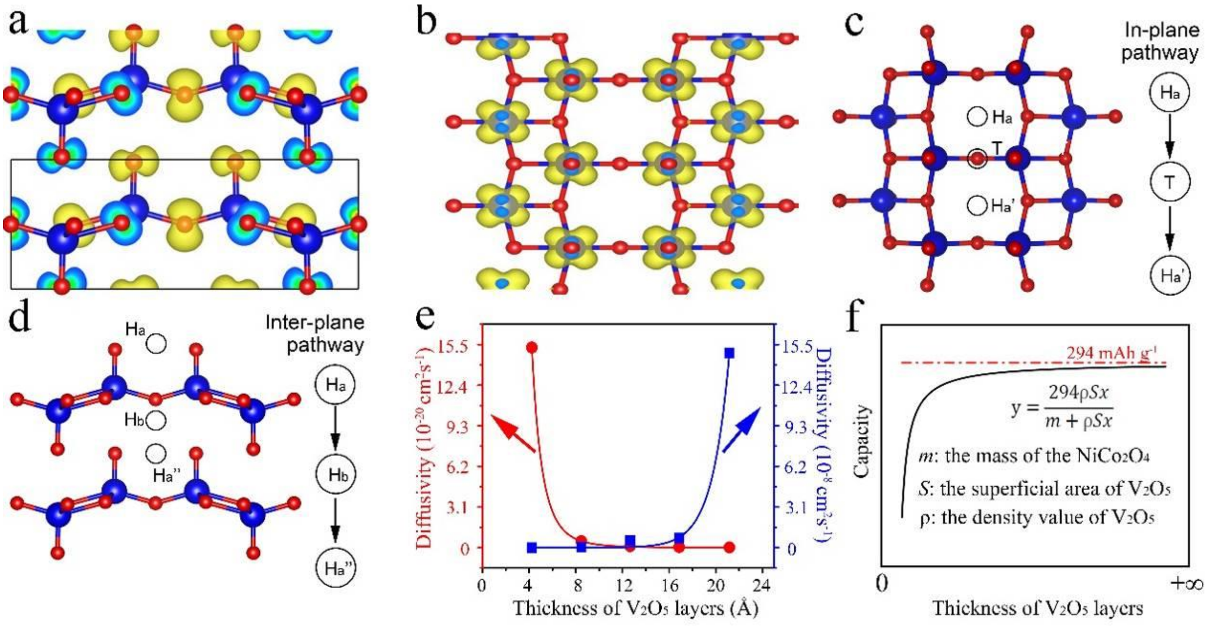

Figure 5. Optimal energy storage performances design analysis from Li diffusivity. (a, b) The side-view and top-view of α-V_2O_5 with the partial charge density of the valence band maximum (a) and conduction band minimum (b). The isosurface is set to 0.01 e/a_0^3. (blue ball: vanadium atom, red ball: oxygen atom) (c, d) Diagrams of the two possible pathways for Li within layered α-V_2O_5. (c) in-plane pathway from hollow position (H_a) to another hollow position ($H^{'}_{a}$) through top position (T); (d) inter-plane pathway from the hollow position in the upper layer (H_a) to the lower layer ($H_a^{''}$); (e) The diffusivity of Li through in-plane (blue line) and inter-plane (red line) pathways as a function of the thickness of α-V_2O_5; (f) theoretical relationship of specific capacity with the change of the thickness of the layered α-V_2O_5 assuming the case of two Li intercalation/de-intercalation.

The table of contents entry

The targeted functional 3D $NiCo_2O_4@V_2O_5$ core-shell sandwich arrays on carbon cloth for rechargeable Li-ion battery have realized theoretical limits of specific capacity and high stability over 500 cycles. The superb performance relies on its structural nano-architecture by separated pathways for lithiation process and conduction. The thickness of the active material is optimized, guided by theoretical study.

Keyword: 3D sandwich arrays, Li-ion battery, Cathodes, Density Functional Theory (DFT), *In-situ* TEM

Title

A Targeted Functional Design for Highly Efficient and Stable Cathodes for Rechargeable Li-Ion Batteries

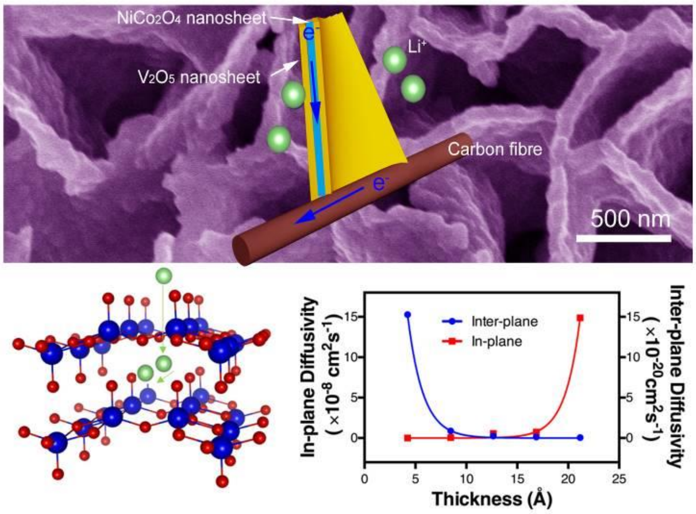

Supporting Information

for *Adv. Mater.*, DOI: 10.1002/adma.((please add manuscript number))

A Targeted Functional Design for Highly Efficient and Stable Cathodes for Rechargeable Li-Ion Batteries

Guanjie He[a,c], Xiaoyu Han[a], Rujia Zou[b,], Tingting Zhao[a], Zhe Weng[c], SocMan Ho-Kimura[a], Yao Lu[a], Hailiang Wang[c], Zheng Xiao Guo[a] and Ivan P. Parkin[a,]**

Guanjie He, Dr. Xiaoyu Han, Tingting Zhao, Dr. SocMan Ho-Kimura, Yao Lu, Prof. Zheng Xiao Guo, Prof. Ivan P. Parkin

[a]Christopher Ingold Laboratory, Department of Chemistry, University College London, 20 Gordon Street, London WC1H 0AJ, U.K.,

E-mail:i.p.parkin@ucl.ac.uk

Prof. Rujia Zou

[b]State Key Laboratory for Modification of Chemical Fibers and Polymer Materials, College of Materials Science and Engineering, Donghua University, Shanghai 201620, China, E-mail:rjzou@dhu.edu.cn

Guanjie He, Dr. Zhe Weng, Prof. Hailiang Wang

[c]Department of Chemistry and Energy Sciences Institute, Yale University, 810 West Campus Drive, West Haven, Connecticut 06516, U.S.A.

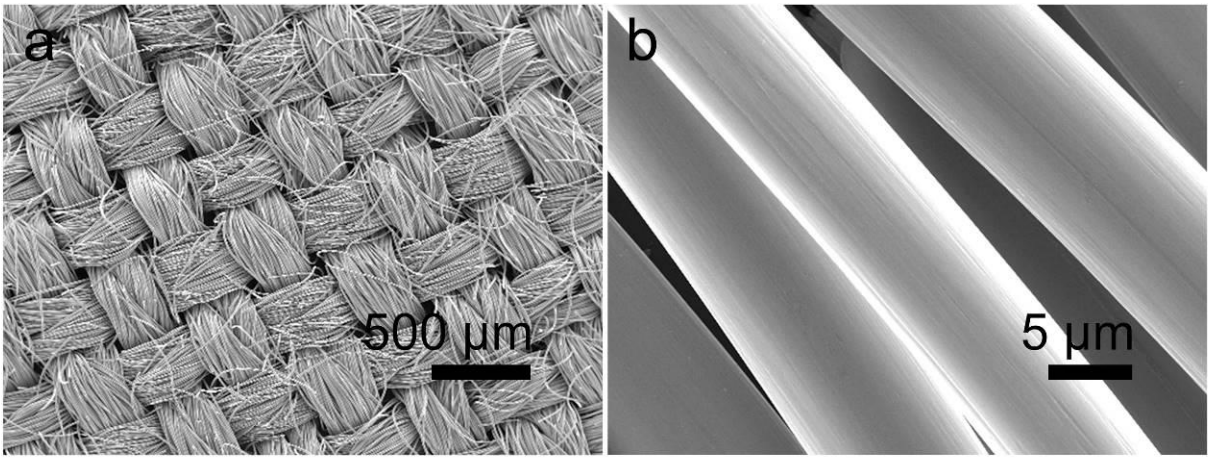

Figure S1. Low and high magnification SEM of the carbon cloth.

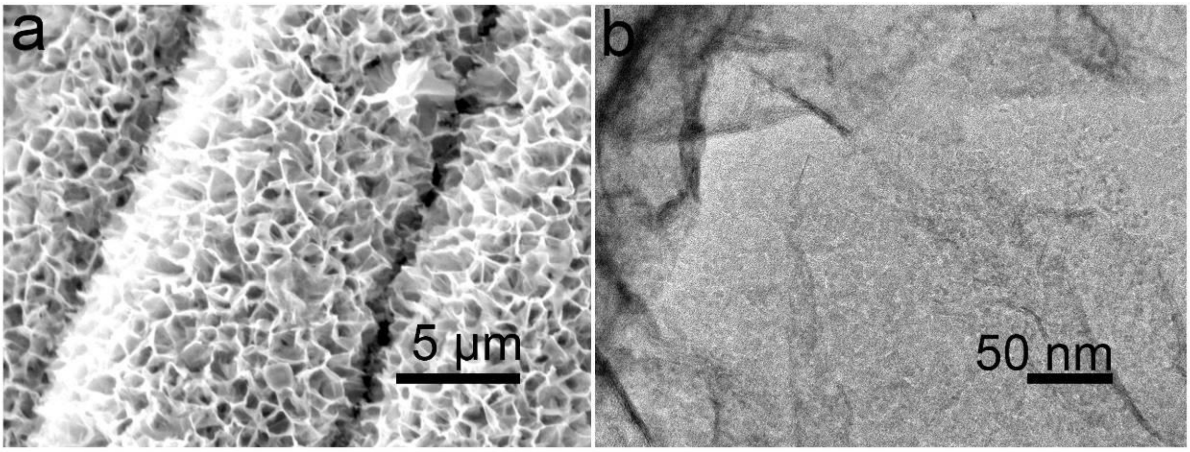

Figure S2. (a) SEM image of the $NiCo_2O_4$ nanoarrays/carbon cloth; (b) TEM images of $NiCo_2O_4$ nanosheet.

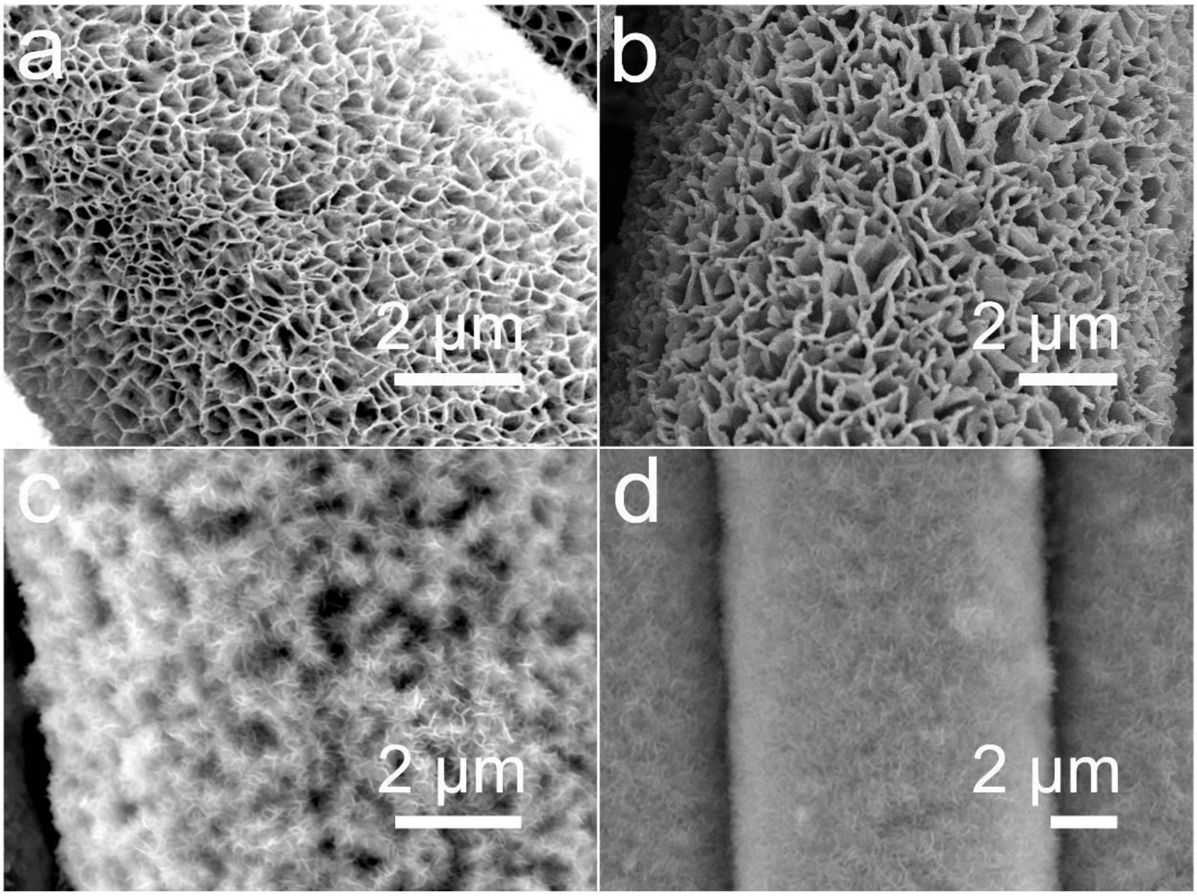

Figure S3. Low magnification SEM image of four kinds of $NiCo_2O_4@V_2O_5$ CSAs/carbon cloth.

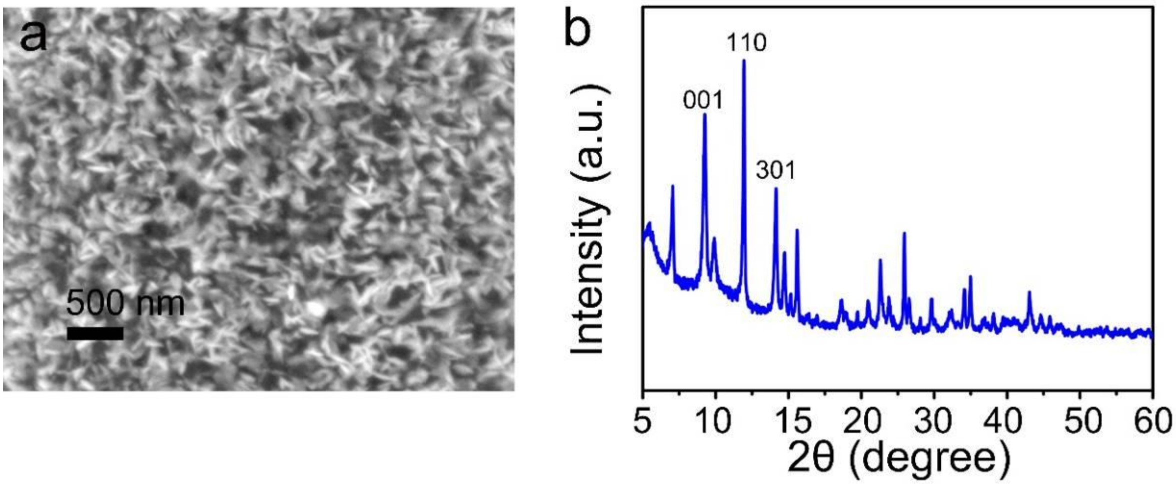

Figure S4. (a) SEM image of V_2O_5 nanoparticles; (b) XRD pattern of V_2O_5 nanoparticles.

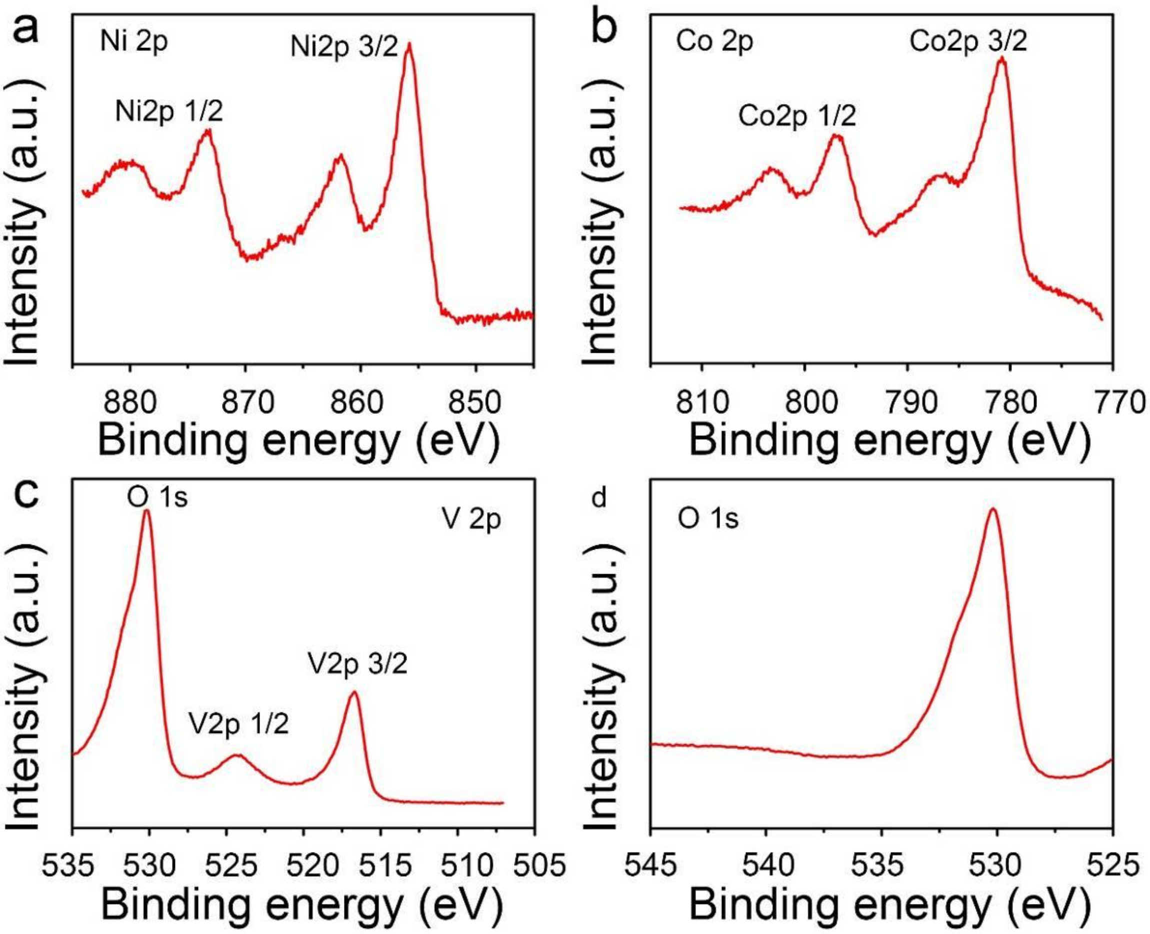

Figure S5. XPS spectra of (a) Ni 2p; (b) Co 2p; (c) V 2p and (d) O 1s.

Table S1. Comparison of energy storage performances of $NiCo_2O_4$@V_2O_5 SAs/carbon cloth as cathodes in LIBs with the representative cathodes in the literature.

Cathodes for LIBs	Specific capacity (Current density)	Rate performances (Increased current density)	Stability	Ref.
$NiCo_2O_4$@V_2O_5 CSAs/carbon cloth	292 mAh g^{-1} (0.1 C)	45% retention (200 times)	0.0126% decrease per cycle (500 cyles at 10 C)	This work
V_2O_5 nanobelts	280 mAh g^{-1} (0.2 C)	32% retention (200 times)	0.28% decrease per cycle (50 cycles at 0.2 C)	[1]
V_2O_5 @carbon nanotubes	224 mAh g^{-1} (0.1 C)	40.2% retention (1000 times)	0.0415% decrease per cycle (200 cycle at 0.5 C)	[2]
Porous V_2O_5 microspheres	275 mAh g^{-1} (0.125 C)	33.5% retention (120 times)	0.38% decrease per cycle (20 cycles at 0.2 C)	[3]
V^{4+}-V_2O_5 nanoflake	293 mAh g^{-1} (100 mA g^{-1})	47.4 % retention (40 times)	0.05% decrease per cycle (100 cycles at 2000 mAh g^{-1})	[4]
V_2O_5 nanosheets	141 mAh g^{-1} (100 mA g^{-1})	88% retention (60 times)	0.09% decrease per cycle (100 cycles at 100 mAh g^{-1})	[5]
$LiNi_{0.4}Mn_{0.4}Co_{0.2}O_2$ spherical particles	228 mAh g^{-1} (0.05 C)	___________	0.2% decrease per cycle (20 cycles)	[6]
V_2O_5 nanoparticles	285 mAh g^{-1} (0.5 C)	62.4% retention (40 times)	0.44% decrease per cycle (50 cycles)	[7]
V_2O_5/graphene	432 mAh g^{-1} (0.05 C)	45.8% retention (200 times)	0.13% decrease per cycle (200 cycles at 1 C)	[8]
$Li_4Mn_2O_5$ composition	355 mAh g^{-1} (0.05 C)	___________	3.7% decrease per cycle (8 cycles)	[9]
Hydrogenated V_2O_5 nanosheets	252 mAh g^{-1} (0.1 A g^{-1})	54.8% retention (20 times)	0.42% decrease per cycle (200 cycles at 0.1 A g^{-1})	[10]

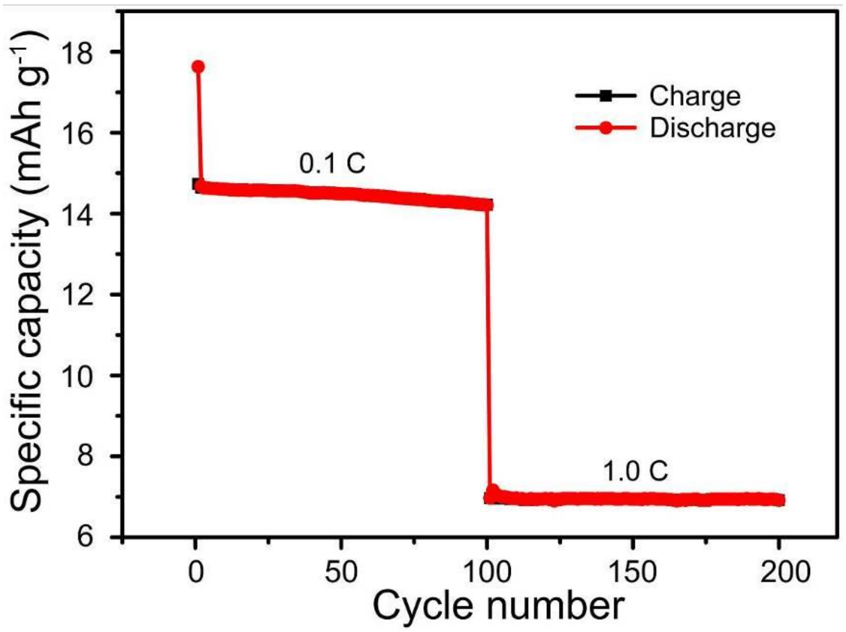

Figure S6. Rate capability of carbon clothes supported $NiCo_2O_4$ nanosheet arrays.

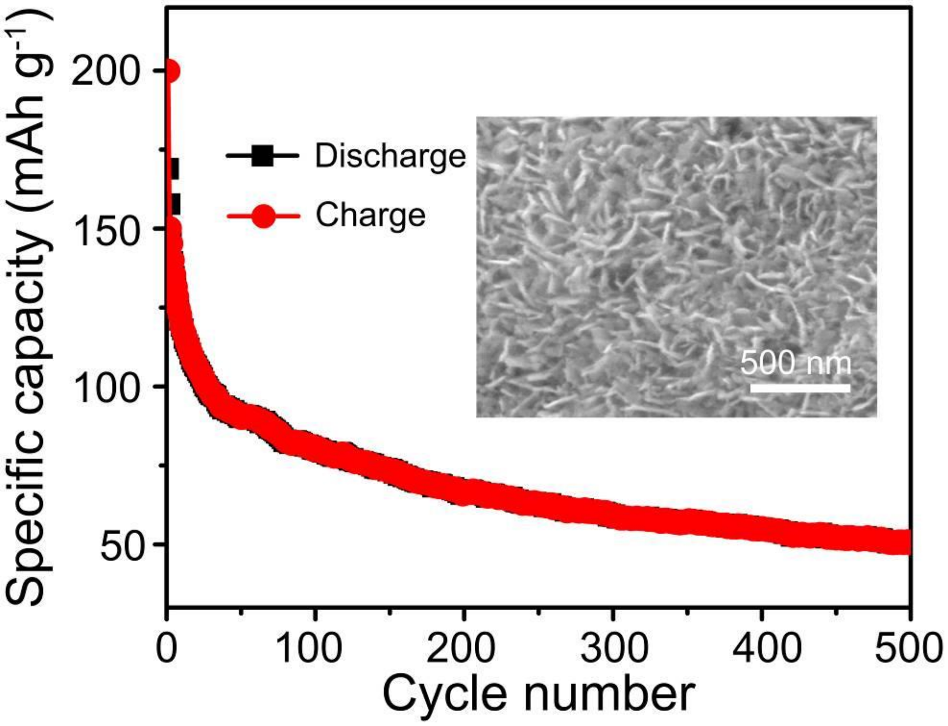

Figure S7. Cycling stability test of the V_2O_5 nanoflowers on carbon cloth at high current density of 10 C, inset showing the SEM image of the V_2O_5 nanoflowers on carbon clothes.

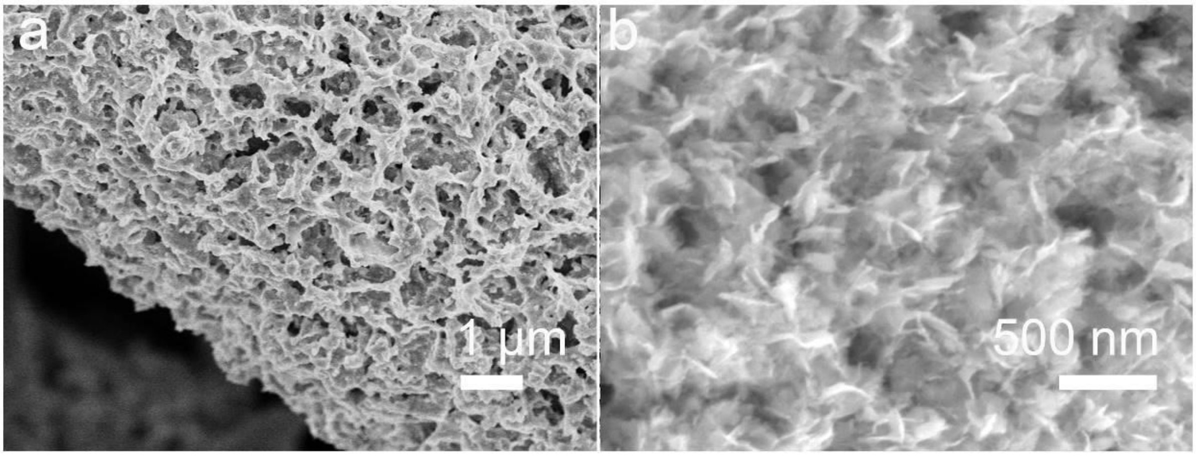

Figure S8. SEM images of $NiCo_2O_4@V_2O_5$ CSAs/carbon cloth and V_2O_5 nanoparticles after 500 cycles at the high current density of 10 C.

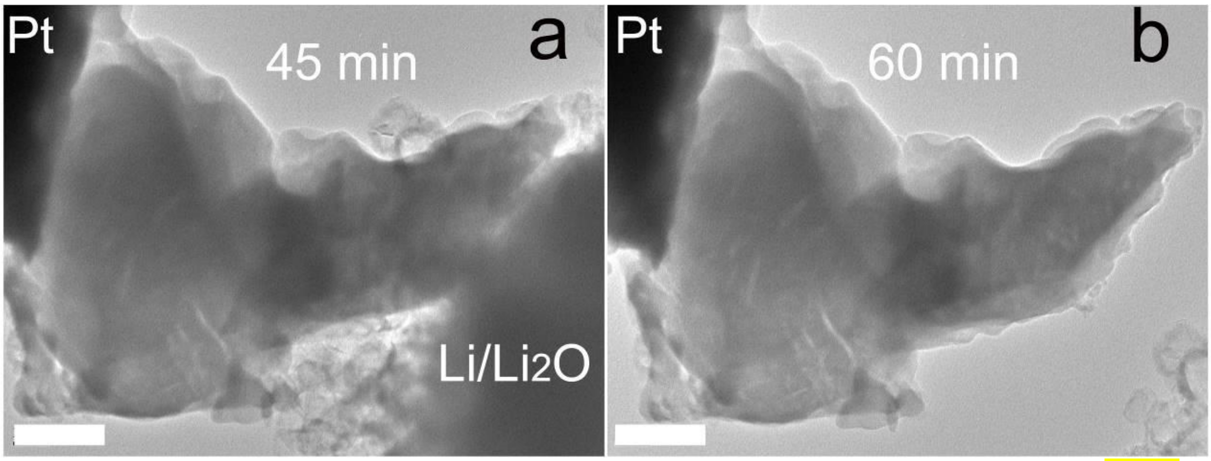

Figure S9. TEM images monitoring the de-lithiation process of the $NiCo_2O_4@V_2O_5$ CSAs at time equal to 45 and 60 min, respectively (Scale bar: 500 nm).

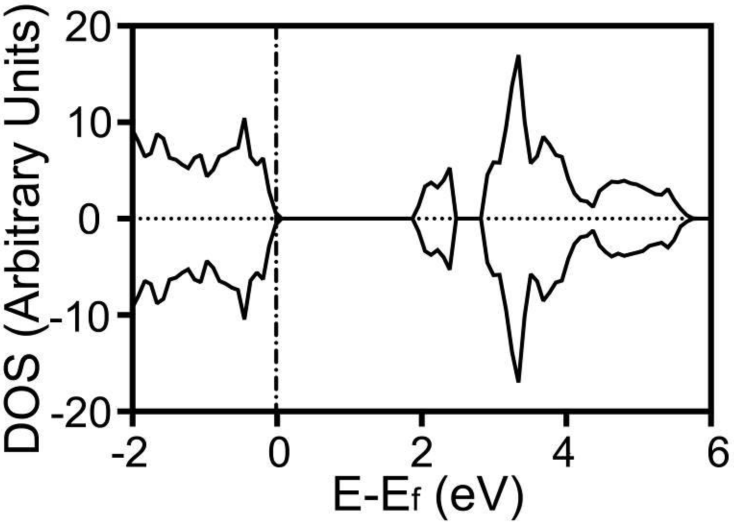

Figure S10. Calculated electronic density of states (DOS) and band structure of α-V_2O_5.

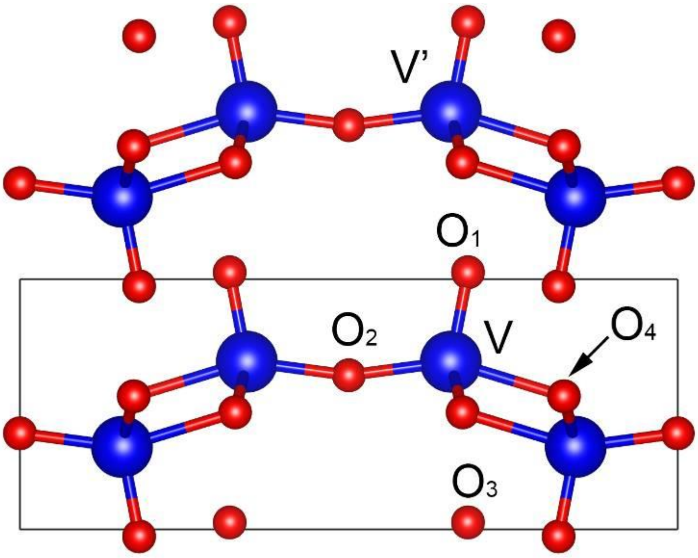

Figure S11. Side-view of two-layer α-V_2O_5 structure, where the V-O bonds denoted.

Table S2. Comparison of different functional and van der Waals correction of lattice parameters and V-O bond distances of bulk α-V_2O_5 (Figure S10), as well as other simulation results and experimental data. The theoretical error is calculated based on experimental work.

	a	**b**	**c**	**V-O$_1$**	**V-O$_2$**	**V-O$_3$**	**V-O$_4$**	**V’-O$_1$**
	This work							
PBEsol-vdW-DF	11.567	3.581	4.392	1.606	1.793	1.884	2.036	2.786
error	0.47%	0.48%	0.55%	1.58%	0.73%	0.16%	0.69%	-0.25%
PBE- vdW-DF2	11.833	3.663	4.493	1.624	1.824	1.927	2.091	2.870
optPBE-vdW	11.648	3.606	4.422	1.609	1.802	1.897	2.048	2.814
	Comparison							
Theoretical work[11]	11.690	3.628	4.423	1.620	1.810	1.912	2.046	2.804
error	1.55%	1.80%	1.26%	2.47%	1.69%	1.65%	1.19%	0.39%
Theoretical work[12]	11.496	3.630	4.804	1.602	1.805	1.915	2.018	3.204
error	-0.14%	1.85%	9.98%	1.33%	1.40%	1.81%	-0.20%	14.7%
Experimental work[13]	11.512	3.564	4.368	1.581	1.780	1.881	2.022	2.793

Table S3. The binding energy (eV) of 1-5 layer α-V_2O_5 at nH_a, nH_b and nT sites, where n represent the layers. The H_a, H_b, and T sites are shown in Figure 5c and d.

	1-Layer	2-Layer	3-Layer	4-Layer	5-Layer
$1H_a$	-2.76	-2.81	-2.81	-2.81	-2.80
$1H_b$	-1.40	-1.47	-1.45	-1.45	-1.35
1T	-2.41	-2.44	-2.42	-2.28	-2.80
$2H_a$		-2.69	-2.71	-2.69	-2.70
$2H_b$		-1.59	-1.66	-1.64	-1.65
2T		-2.53	-2.66	-2.67	-2.66
$3H_a$			-2.74	-2.74	-2.76
$3H_b$			-1.59	-1.66	-1.60
3T			-2.37	-2.58	-2.58
$4H_a$				-2.73	-2.74
$4H_b$				-1.60	-1.62
4T				-2.36	-2.36
$5H_a$					-2.74
$5H_b$					-1.60
5T					-2.39

Table S4. Simulated values of the Li diffusivity within layered α-V_2O_5.

Atom layers of V_2O_5	Inter-plane pathway ($cm^2\ s^{-1}$)	In-plane pathway ($cm^2\ s^{-1}$)
1	1.53×10^{-19}	2.03×10^{-11}
2	8.80×10^{-21}	5.26×10^{-10}
3	2.49×10^{-21}	5.53×10^{-9}
4	1.15×10^{-21}	7.31×10^{-9}
5	5.34×10^{-22}	1.49×10^{-7}

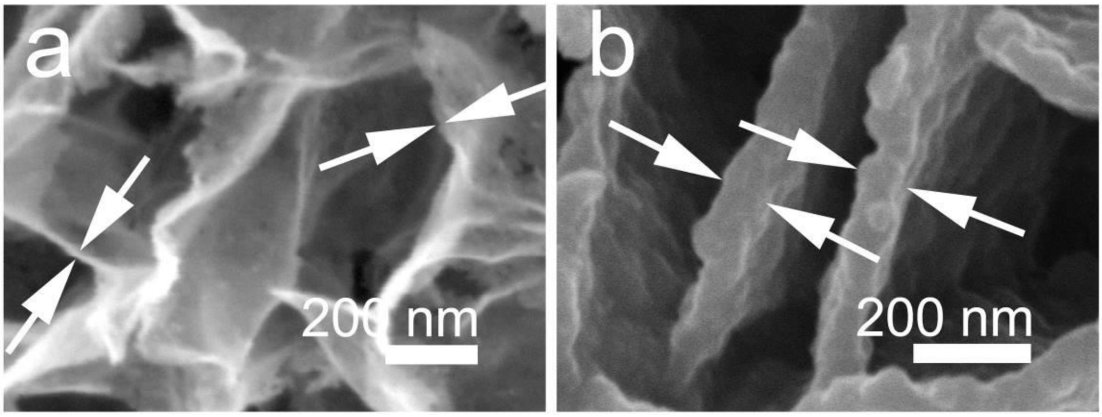

Figure S12. High magnification SEM of (a) 3D $NiCo_2O_4$ nanosheets on carbon cloth; (b) $NiCo_2O_4@V_2O_5$ CSAs/carbon cloth.

From the SEM images:
The average thickness of the $NiCo_2O_4$ nanosheets is *ca.* 21.1 nm
The average thickness of the $NiCo_2O_4@V_2O_5$ CSAs is *ca.* 86.3 nm

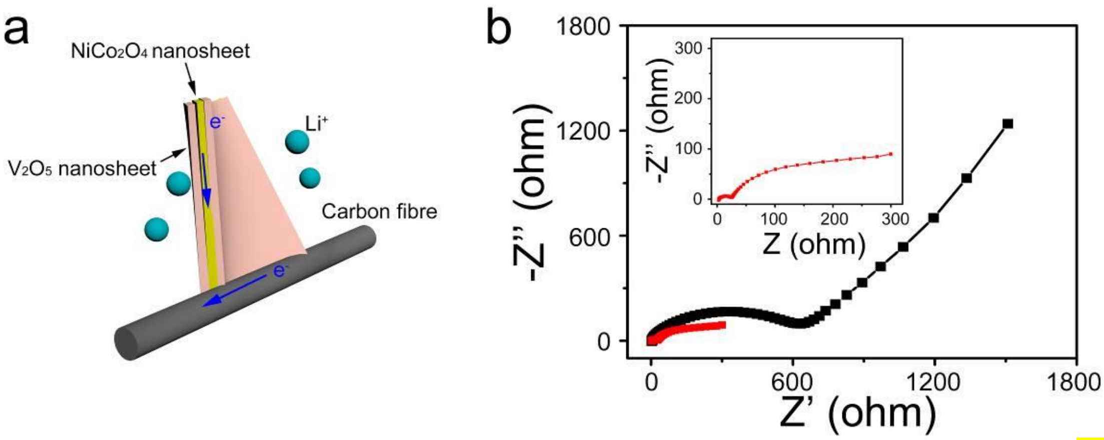

Figure S13. (a) Schematic illustration of electrochemical reactions of $NiCo_2O_4@V_2O_5$ CSAs; (b) EIS spectra of $NiCo_2O_4@V_2O_5$ CSAs/carbon cloth (red line) and V_2O_5 nanoparticles (black line).

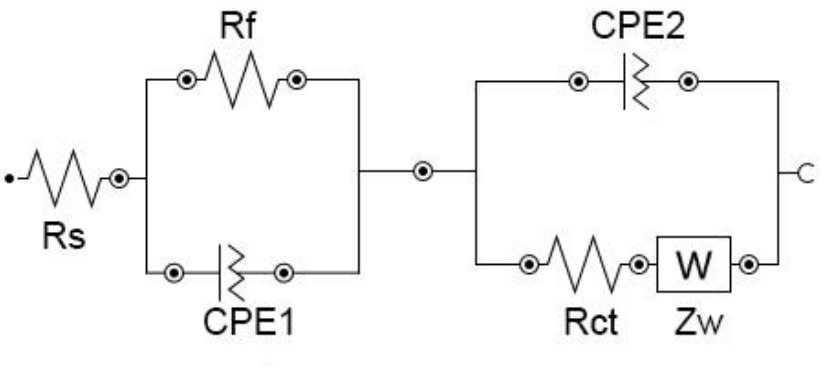

Figure S14. Equivalent circuit model of $NiCo_2O_4@V_2O_5$ CSAs/carbon cloth and V_2O_5 nanostructure electrodes.

In the above equivalent circuit model, Rs is the electrolyte resistance; CPE1 and Rf are the capacitance and resistance of the passivation SEI film formed on the electrode surfaces, respectively; CPE2 and Rct are the double-layer capacitance and charge transfer resistance, respectively; and Zw is the Warburg impedance in regard to the diffusion of Li into the bulk of the electrode.

Table S5. Parameters from the equivalent circuit model.

Electrodes Parameters	$NiCo_2O_4@V_2O_5$ SAs/carbon cloth	V_2O_5 nanoparticles
R_f (Ω)	21.3	104
R_{ct} (Ω)	223	454
R_s (Ω)	2.87	3.14

Experimental Section

Sample Preparation. All chemicals used in this work are commercially available from Sigma-Aldrich (UK) and were used as-received without further purification. The $NiCo_2O_4@V_2O_5$ CSAs were synthesized on carbon cloth using a two-step hydrothermal reaction combined with annealing. Firstly, $Co(NO_3)_2•6H_2O$ (0.58 g), $Ni(NO_3)_2•6H_2O$ (0.29 g) and methenamine (0.56 g) were dissolved into a solution of methanol (35 mL) to form a clear pink solution. The carbon cloth substrates were cleaned by sonication in acetone, deionized (DI) water and ethanol for 30 min sequentially, and then transferred into the autoclave with the above pink solution in an electrical oven at 160 ˚C for 6 h. After the reaction, the NiCo-hydrate on carbon cloth was annealed at 300 ^oC for 2 h under air in the tube furnace. Four pieces of carbon cloth were prepared in the first step. Secondly, different amounts of vanadium oxytriisopropoxide (0.1 ml, 0.2 ml, 0.4 ml and 0.6 ml) were added into isopropanol alcohol (50 mL) in four separate beakers under vigorous stirring for 30 min. The mixture solution was transferred into four 60 mL teflon-lined autoclaves with one piece of $NiCo_2O_4$ nanosheet arrays coated carbon cloth, which was sealed and heated in an electrical oven at 200 ^oC for 12 h. Then, the as-synthesized materials on carbon clothes were washed with DI water and ethanol to remove any loosely attached powders and remove any residual ionic species and dried in a vacuum oven at 60 ^oC for 24 h. At last, the as-synthesized samples on carbon clothes were annealed at 350 ^oC for 2 h under air in the tube furnace.

Characterization. Morphology and microstructure of the as-synthesized samples were characterized by SEM (S-4800; Hitachi) and TEM (JEOL, JEM-2100F equipped with an energy-dispersive X-ray spectrometer). X-ray diffraction patterns were recorded using a STOE StadiP diffractometer with Mo-Kα radiation (λ = 0.71 Å). The surface chemical structures were evaluated using an X-ray photoelectron spectroscopy (XPS; Thermo scientific K-alpha photoelectron spectrometer). The mass of the active materials was weighed using the accurate balance (readability of 0.001 mg). *In-situ* TEM observation of the lithiation process was performed using a scanning tunneling microscopy-TEM holder from Nanofactory Instruments AB (Gothenburg, Sweden) within the JEOL 2100F TEM, which was operated at 200 kV.

Electrochemical measurements. The $NiCo_2O_4$@V_2O_5 CSAs/carbon cloth nanocomposites were used as working electrodes directly without adding any conductive agents or binder materials. The loading densities were calculated as 1.790-1.816, 2.594-2.618, 3.040-3.072, 3.640-3.812 mg/cm^2 for the four kinds of samples, the $NiCo_2O_4$ nanosheet arrays was 0.994-1.024 mg/cm^2 on the carbon clothes. The V_2O_5/carbon clothes is loaded with ~1.76 mg/cm^2 of V_2O_5. The mass of the carbon cloth in each coin cell is ~ 18 mg. With regards to the comparison electrodes preparation, the working electrode was prepared by mixing the V_2O_5 nano-flowers (SEM image, Figure. S4a and XRD patterns, Figure. S4b), conductive agent (carbon black) and binder (sodium alginate) with a weight ratio of 50:40:10. Coin-type cells (CR2032) were fabricated using lithium metal as the counter electrode, Celgard 2400 (Charlotte, NC, USA) as the separator and 200 μL of 50 $LiPF_6$ (1 M) in ethylene carbonate-dimethyl carbonate (1:1 vol%) as the electrolyte. Cyclic voltammetry (CV) measurements were conducted at 0.1 mV s^{-1} in the range of 2.0 ~ 4.0 V (*vs.* Li/Li$^+$) on a CHI 600D

(Shanghai, China) electrochemical workstation. Electrochemical impedance spectroscopy was carried out with a ZAHNERelektrik IM 6 (Kronach) electrochemical system at a frequency range of 100 kHz to 0.01Hz. All the electrochemical measurements were tested more than twice to ensure the replication of the results.

Theoretical methods of layer effect on lithiation in V_2O_5. DFT+U calculations were performed using a projector-augment wave (PAW) pseudopotential, implanted in the Vienna *Ab initio* Simulation Package(VASP).[14] As the van der Waals interaction dominant the intra-layer of α-V_2O_5, serial functions have been adopted for comparison, including PBEsol-vdW-DF, PBE-vdW-DF2, and optPBE-vdW.[12, 15-21] The plane-wave basis set with energy cut-off of 520 eV. The Brillouin zone was sampled by Gamma centred 2 × 2 × 2 k-mesh for the bulk and 2 × 2 × 1 for the layered slides. All structures were fully relaxed until the force on each atom was less than 0.01 eVÅ^{-1}. Spin polarization counted through all the simulations. Due to the limitation of DFT calculations in presenting the delocalised *d* and *f* electrons excessively,[22] the effective Coulomb and exchange parameters +U was set to 4 eV as suggested in previous theoretical calculations.[23]

The 2a × 2b supercell of 1- to 5-layer α-V_2O_5 have adopted for the analysis of the layer effect on Li intra-plane and inter-plane diffusion process. Dipole correction has adopted through all the calculations. For the few-layer V_2O_5, each model has 15 Å vacuum region. Energy barrier of the Li were calculated by Climbing Image Nudged Elastic Band (Ci-NEB) method.[24]

References

[1] X. Rui, Y. Tang, O. I. Malyi, A. Gusak, Y. Zhang, Z. Niu, H. T. Tan, C. Persson, X. Chen, Z. Chen, Q. Yan, *Nano Energy* **2016**, *22*, 583-593.

[2] D. Kong, X. Li, Y. Zhang, X. Hai, B. Wang, X. Qiu, Q. Song, Q.-H. Yang, L. Zhi, *Energy Environ. Sci.* **2016**, *9*, 906-911.

[3] S. Wang, Z. Lu, D. Wang, C. Li, C. Chen, Y. Yin, *J. Mater. Chem.* **2011**, *21*, 6365.

[4] H. Song, C. Liu, C. Zhang, G. Cao, *Nano Energy* **2016**, *22*, 1-10.

[5] H. Song, C. Zhang, Y. Liu, C. Liu, X. Nan, G. Cao, *J. Power Sources* **2015**, *294*, 1-7.

[6] F. Lin, D. Nordlund, Y. Li, M. K. Quan, L. Cheng, T.-C. Weng, Y. Liu, H. L. Xin, M. M. Doeff, *Nature Energy* **2016**, *1*, 15004.

[7] T. Kim, J. Shin, T.-S. You, H. Lee, J. Kim, *Electrochim. Acta* **2015**, *164*, 227-234.

[8] Q. Liu, Z. F. Li, Y. Liu, H. Zhang, Y. Ren, C. J. Sun, W. Lu, Y. Zhou, L. Stanciu, E. A. Stach, J. Xie, *Nat. Commun.* **2015**, *6*, 6127.

[9] M. Freire, N. V. Kosova, C. Jordy, D. Chateigner, O. I. Lebedev, A. Maignan, V. Pralong, *Nat. Mater.* **2016**, *15*, 173-177.

[10] X. Peng, X. Zhang, L. Wang, L. Hu, S. H.-S. Cheng, C. Huang, B. Gao, F. Ma, K. Huo, P. K. Chu, *Adv. Funct. Mater.* **2016**, *26*, 784-791.

[11] J. Carrasco, *J. Phys. Chem. C* **2014**, *118*, 19599-19607.

[12] D. O. Scanlon, A. Walsh, B. J. Morgan, G. W. Watson, *J. Phys. Chem. C* **2008**, *112*, 9903-9911.

[13] R. Enjalbert, J. A. Galy, *Acta Crystallogr. C* **1986**, *C42*, 1467-1469.

[14] G. Kresse, J. Furthmuller, *Phys. Rev. B* **1996**, *54*, 169-186.

[15] J. P. Perdew, J. A. Chevary, S. H. Vosko, K. A. Jackson, M. R. Pederson, D. J. Singh, C. Fiolhais, *Phys. Rev. B* **1992**, *46*, 6671-6687.

[16] K. Lee, É. D. Murray, L. Kong, B. I. Lundqvist, D. C. Langreth, *Phys. Rev. B* **2010**, *82*, 081101(R).

[17] T. Thonhauser, V. R. Cooper, S. Li, A. Puzder, P. Hyldgaard, D. C. Langreth, *Phys. Rev. B* **2007**, *76*, 125112.

[18] M. Dion, H. Rydberg, E. Schroder, D. C. Langreth, B. I. Lundqvist, *Phys. Rev. Lett.* **2004**, *92*, 246401.

[19] J. Klimes, D. R. Bowler, A. Michaelides, *J. Phys. Condens. Matter.* **2010**, *22*, 022201.

[20] J. Klimeš, D. R. Bowler, A. Michaelides, *Phys. Rev. B* **2011**, *83*, 195131.

[21] G. Roman-Perez, J. M. Soler, *Phys. Rev. Lett.* **2009**, *103*, 096102.

[22] S. Fabris, S. de Gironcoli, S. Baroni, G. Vicario, G. Balducci, *Phys. Rev. B* **2005**, *72*, 041102(R).

[23] G. Henkelman, B. P. Uberuaga, H. Jónsson, *J. Phys. Chem.* **2000**, *113*, 9901.

[24] J. P. Perdew, A. Ruzsinszky, G. I. Csonka, O. A. Vydrov, G. E. Scuseria, L. A. Constantin, X. Zhou, K. Burke, *Phys. Rev. Lett.* **2008**, *100*, 136406.